Available online at www.sciencedirect.com
SCIENCE DIRECT®
ELSEVIER
International Journal of Solids and Structures 43 (2006) 4384–4406
INTERNATIONAL JOURNAL OF SOLIDS and STRUCTURES
www.elsevier.com/locate/ijsolstr

Parametric studies of failure mechanisms in elastic EB-PVD thermal barrier coatings using FEM

Himanshu Bhatnagar, Somnath Ghosh *, Mark E. Walter

Department of Mechanical Engineering, The Ohio State University, 650 Ackerman Rd., Columbus, OH 43202, United States

Received 8 March 2005; received in revised form 26 June 2005
Available online 22 September 2005

Abstract

Catastrophic failure of thermal barrier coatings (TBCs), usually occurs due to large scale buckling and spallation, primarily originating at the bond coat and TGO interface. Spallation in TBCs is preceded by a competition between buckling and interface delamination that is stimulated by the waviness of the interface. In the presence of thermal loading, the waviness is responsible for growth of interfacial delamination. In this paper, a finite element model of the two and three layer TBC's is developed in the commercial code ANSYS to investigate the buckle and interface delamination mechanisms and develop a simplified parametric understanding of these mechanisms. The models for simulation are validated with analytical and experimental results. Parametric relations, in terms of geometric and material parameters representing constituents of the TBC, are developed in this paper for critical stresses and energies causing buckling and debonding initiated instabilities. Through these relations, critical parameters that control failure mechanics are identified for a fail-safe design space.

Keywords: Thermal barrier coatings; Failure mechanisms; Parametric formalism; Buckling instability; Interfacial crack extension; Energy release rate; Sensitivity analysis

1. Introduction

Electron beam physical vapor deposition (EB-PVD) based thermal barrier coatings (TBCs) are used in gas turbine engines to protect components from high temperature gases and severe transient thermal loading. As shown in the SEM micrograph of Fig. 1, a conventional TBC consists of three layers deposited on a super alloy substrate. The first layer is a 50–100 μm thick bond coat that provides oxidation protection,

* Corresponding author. Tel.: +1 614 292 2599; fax: +1 614 292 7369.
E-mail address: ghosh.5@osu.edu (S. Ghosh).

0020-7683/$ - see front matter © 2005 Elsevier Ltd. All rights reserved.
doi:10.1016/j.ijsolstr.2005.07.037

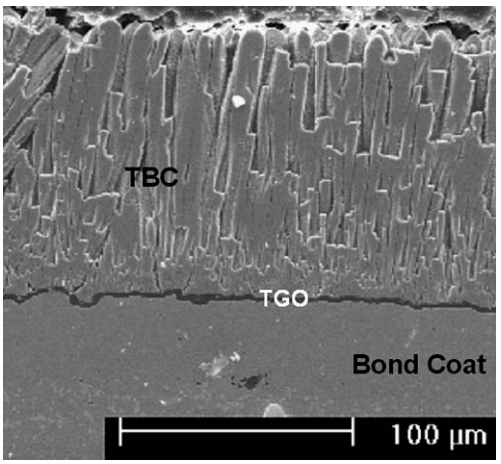

Fig. 1. A SEM image of the TBC microstructure consisting of the top coat, the thermally grown oxide layer, the bond coat and the super-alloy substrate.

while the second is a 100–120 μm thick top coat for providing thermal insulation. The top coat is structured to be strain tolerant to avoid delamination; this is achieved by incorporating micro-cracks or aligned porosity in the material as suggested by Wright and Evans (1999). Typically, due to its low, temperature-insensitive thermal conductivity (Wright and Evans, 1999), yittria stabilized Zirconia is the material of choice for the top coat. The porous nature of the top coat makes it transparent to oxygen, and thus a third layer is formed as the bond coat is oxidized. This thermally grown oxide (TGO) layer retards further oxidation and improves adhesion (Wright and Evans, 1999). The TGO thickness evolves through the life of the TBC and typically reaches 6–7 μm before failure (Tolpygo et al., 2001). As shown in Fig. 1, the SEM images of the TBC microstructure reveal the interface between the TGO and bond coat may be planar or wavy.

Individual layers in TBCs are significantly stronger than the inter-layer interfaces. Furthermore the interface toughness also tends to degrade with exposure time. Consequently, over their service life, TBCs are susceptible to delamination. Experimental observations by Wang and Evans (1998) have confirmed that the delamination leads to buckling instability and failure in TBCs. On account of their importance in the overall durability of the engine components, modeling buckling and delamination phenomena are of considerable interest to the engineering community. Stresses developed due to the coefficient of thermal expansion (CTE) mismatch between the different layers during thermal loading, as well as growth stresses in the TGO are the primary driving forces behind the initiation and propagation of damage. Evans et al. (2001b) have reported that the residual compressive stresses in the TGO can reach up to 6 GPa.

A number of geometrical and mechanical factors are known to contribute to the instability and failure in TBCs. Notable among these are important geometric and morphological features of interfaces and constituent layers, and their thermo-mechanical properties. On a flat interface, the spallation failure is primarily driven by local buckling instability at the delamination site. A significant body of work exists in the literature on this failure mechanism with the details of buckle initiation, propagation, and coalescence (Evans et al., 1997; He et al., 1998; Hutchinson et al., 2000; Hutchinson and Suo, 1992; Choi et al., 1999). A number of these investigations in the literature consider a two layer TBC system, where the substrate is coated with a bond coat layer and no ceramic top coat is deposited. A widely used analytical solution for critical buckling load for a circular blister has been developed by Hutchinson and Suo (1992), and this solution has been employed to predict buckle initiation in TBCs by Evans et al. (1997) and He et al. (1998). The analytical model by Hutchinson and Suo (1992) is based on classical plate theory with rotationally constrained edges. While this model is accurate for very large interfacial delamination, the predictions incur error for the insipient

stages of delamination where the assumed rotational constraints are questionable. The presence of interfacial waviness dramatically affects failure mechanisms in TBCs. This has been highlighted Evans et al. (1997), where a sinusoidal undulation was used to understand the origin of interfacial cracks and by He et al. (1998), where crack growth along the interface has been associated with periodic and a-periodic morphologies. The onset of failure in TBCs may consequently be viewed as a competition between strain energy driven interfacial crack growth mechanism and buckling induced instability and delamination.

This paper is aimed at the development of parametric formalism through the numerical study of instability and failure mechanisms in TBC systems by using the finite element method. A few simplifying assumptions have been made in the derivation of the closed-form parametric relations. One of them is that the TBC model consists of no defects in the form of other heterogeneities, such as voids or particles. The existence and creation of these defects, together with their influence on TBC failure have been discussed in details in a paper by Yanar et al. (2003). However, the present paper has made an assumption of excluding these for the sake of developing closed-form parametric relations to be used in design assessments. Interfaces between different layers of the TBC systems are assumed to consist of planar (with delaminations) and wavy (undergoing imminent delamination) segments. A schematic of the competing damage modes due to pre-existing delamination at the TGO-bond coat interface is shown in Fig. 2. The parametric relations are constructed to evaluate critical factors affecting buckling initiation and interface crack extension, as well as to understand the competition between them. These relations are expected to be applicable to TBC systems with geometric and material parameters within the specified range. The computational model assumes the substrate to be rigid, and excludes its explicit consideration in the deformation and stress analyses. The bond coat and TGO are analyzed using elastic properties, and the model features a pre-existing delamination at the interface of bond coat and TGO. In the sensitivity analysis of candidate parameters, each failure mechanism is studied in isolation from other mechanisms. In the analysis, a linear elastic eigen-value problem is solved as explained in Ansys 7.0 (2003) to determine the initiation of buckling instability. For estimating the crack propagation at the interface, the energy release rate is determined by the virtual crack extension method based on the stiffness derivative finite element technique proposed by Parks (1974).

The paper starts with a focus on buckling delamination, where the contribution of material and geometric parameters to buckling initiation in two layer TBCs is estimated. A parametric relationship for the critical buckling load in terms of the parameters is developed and compared with existing analytical solutions in the literature for a two layer TBC model. Also the amount of pre-existing delamination that is necessary

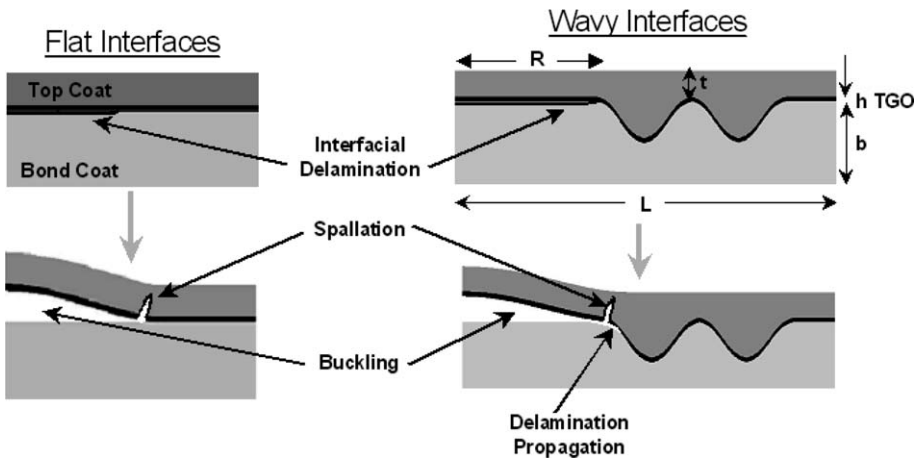

Fig. 2. Schematic diagrams showing the competing failure mechanisms in TBC systems with flat and wavy interfaces.

for the initiation of buckling instability is determined for applied compressive stresses in the TGO. A similar process is also executed for three layer TBCs and compared with the results for the two layer TBC to examine the effect of the top coat. Next, a similar approach is pursued to study strain energy driven delamination at wavy interfaces. A sensitivity analysis is conducted to identify important material and geometric parameters affecting the energy release rate for crack propagation at the interface of single layer and multi layer TBCs. As a final step, the critical values of parameters obtained for competing buckling instability and interface delamination mechanisms are compared, to identify dominant mechanism ranges and to prescribe a fail-safe design space.

2. Mechanisms of tbc failure and solution methods

In the context of linear elastic behavior, dominant failure mechanisms in thermal barriers coatings have been identified as the buckling instability and delamination by crack extension along the interface between the bond coat and TGO by Evans et al. (1997), He et al. (1998), Wright and Evans (1999) and Evans et al. (2001a,b). During operation under thermal loads, the TBC can experience critical loads leading to buckling instability and unbounded out-of-plane deflections of the delaminated portion, as shown in the schematic of Fig. 2. The buckling instability is eventually arrested at the edge of delamination by the bonded interface. On the other hand, high stress concentrations at the delamination edges can propagate a crack at the interface to increase the extent of delamination. The probability of a particular mode, taking precedence over the other in a TBC under operating conditions, will depend on various geometric and material parameters affecting each mechanism as well as the applied loading. Hence it is of interest to study the dependence of the variables driving these mechanisms on the TBC parameters. A brief introduction to the methods of solution implemented to study these mechanisms is presented next.

2.1. Buckling instability at flat and wavy interfaces

Irrespective of the interface morphology, the delaminated portion of the TBC is susceptible to buckling instability. In addition to the geometric features and material properties, the nature of the delamination and the critical buckling stresses depend on the contact conditions at the interfaces. A linearized model of elastic stability, using modal analysis in the commercial FEM code ANSYS (Ansys 7.0, 2003), is incorporated to determine the critical buckling stresses in the TBC system. In this model, the effect of in-plane compressive stresses on the out-of-plane deflection is accounted for by a stress stiffness matrix $[\boldsymbol{S}]$ that augments the conventional stiffness matrix $[\boldsymbol{K}]$. As shown in Ansys 7.0 (2003), the $[\boldsymbol{S}]$ matrix is independent of material properties. The stress stiffening matrix $[\boldsymbol{S}]$ is computed from the intensity of the compressive load, referred to as a perturbation stress $\{\boldsymbol{R}\}$, with a linear dependence arising from problem linearity. Assuming that the compressive stress does not change during an infinitesimal change in the buckling displacement $\{\boldsymbol{\Delta D}\}$, the critical load for instability in two contiguous configurations may be equated as (Cook et al., 1989):

$$\boldsymbol{\lambda}_{\mathrm{cr}}\{\boldsymbol{R}\} = ([\boldsymbol{K}] + \boldsymbol{\lambda}_{\mathrm{cr}}[\boldsymbol{S}])\{\boldsymbol{D}\} = ([\boldsymbol{K}] + \boldsymbol{\lambda}_{\mathrm{cr}}[\boldsymbol{S}])\{\boldsymbol{D} + \mathrm{d}\boldsymbol{D}\} \tag{1}$$

where $\{\boldsymbol{D}\}$ is the buckling displacement vector in the reference configuration and λ_{cr} is a scalar multiplier. This is simplified to give the incremental buckling equation as

$$([\boldsymbol{K}] + \boldsymbol{\lambda}_{\mathrm{cr}}[\boldsymbol{S}])\{\mathrm{d}\boldsymbol{D}\} = \{\boldsymbol{0}\} \tag{2}$$

Eq. (2) corresponds to a modal analysis problem with $\{\mathrm{d}\boldsymbol{D}\}$ as the eigenvector and an associated eigenvalue λ_{cr} defining the buckling mode. The block Lanczos eigen-value extraction method is used in ANSYS (Ansys 7.0, 2003) to determine the lowest eigen-value. Subsequently λ_{cr} is used to scale the far field compressive stress in the TGO to determine the critical buckling stress.

2.2. Delamination growth by crack propagation at interfaces

In the model, the applied load is in a direction parallel to the constituent material layers and their associated interfaces. For this load condition, a crack tip at the delaminated flat interface does not induce a stress concentration to cause crack extension. Consequently, crack growth at the interface between the bond coat and TGO interface is studied exclusively for wavy interfaces. In this study, this mechanism is assumed to be governed by Griffith's energy release rate criterion. According to this criterion, crack growth will occur if the energy required for creating new crack surface area is achieved in the system. The virtual crack extension method, based on the stiffness derivative finite element technique proposed by Parks (1974), is used to evaluate the energy release rate. This is determined as the negative of the derivative of the total system potential energy with respect to crack extension. In the finite element model, the potential functional is represented in terms of the global stiffness matrix, the displacement field and the external loads. The energy release rate G is thus expressed by the stiffness derivative technique by Parks (1974) as

$$G = -\frac{\partial U}{\partial a} = -\frac{1}{2}\{\boldsymbol{D}\}^{\mathrm{T}}\frac{\partial[\boldsymbol{K}]}{\partial a}\{\boldsymbol{D}\} \tag{3}$$

where $\{\boldsymbol{D}\}$ is the displacement field, $[\boldsymbol{K}]$ is the stiffness matrix, and a is the crack length. G is evaluated numerically from the change in system potential energy per unit crack extension due to a virtual extension of the crack using the relation:

$$G = -\frac{1}{2}\frac{(U_1 - U_2)}{\Delta a} \tag{4}$$

where U_1 and U_2 are the respective total potential energies before and after the crack extension by length Δa. A FEM analysis is first conducted with a prescribed length of delamination, and the potential energy U_1 of the system associated with the applied load is calculated. In the second analysis to evaluate U_2, the finite element analysis is conducted with the crack extended by an infinitesimal length over the initial delamination.

To eliminate the contribution of structural compliance variation due to crack extension, the strain field computed from the first pre-crack extension model is applied to the second analysis. The virtual crack extension is achieved by moving the FE nodes in the vicinity of the crack tip in the direction of probable crack propagation. The results are sensitive to the region considered as crack tip vicinity and magnitude of crack extension. A very large crack extension may result in distorted elements, whereas, a very small extension may not result in a correct energy release rate. The models used in this study are checked for convergence of the energy release rate with respect to both of these parameters. It is found that variation in energy release rate calculated from the numerical model is within 2% when the nodes associated with at least three layers of nearest and contiguous elements are moved by 1% of the edge length of the elements in close vicinity. The converged values of these parameters are utilized in all subsequent analyses.

3. Finite element models of the TBC

Various aspects of the finite element model of the TBC with different damage mechanisms are summarized in the following subsections.

3.1. Material properties

The EB-PVD TBC system conventionally consists of multiple layers of different materials with distinct interfaces. The substrate is usually a nickel based superalloy with high strength and stiffness, even at

Table 1
Material properties of components of the TBC system as obtained from Evans et al. (2001a,b) and Cheng et al. (1998)

Property	Substrate	Bond coat	TGO	TBC
Poisson's Ratio	0.31–0.35	0.30–0.33	0.23–0.25	0.10–0.12
Elastic modulus (GPa)	120–220	110–200	320–400	0–100
Thermal expansion coefficient (10^{-6}/°C)	14.8–18.0	13.6–17.6	8.0–9.6	9.0–12.2

elevated temperatures. The bond coat material is often an inter-metallic platinum modified nickel aluminide with a CTE similar to that of the substrate material. Mechanical properties of the bond coat material may vary with thermal cycling as reported by Pan et al. (2003). The top coat material of choice is yittria stabilized zirconia with a strain tolerant columnar structure. Johnson et al. (1998) have reported that material properties of the top coat vary with deposition process parameters, as well as with the inter-columnar spacing. The mechanical properties of all the layer materials are obtained from those reported by Evans et al. (2001a,b) and Cheng et al. (1998) and are listed in Table 1. All the materials are assumed to have linear elastic isotropic behavior.

Since the interface is the most likely location for damage, interface toughness in TBCs is of key importance. The interface between the bond coat and the TGO experiences severe stresses due to thermal expansion mismatch and is crucial to TBC durability. The interfacial toughness degrades over time due to segregation (particularly of sulfur) and thermal cyclic loading (He et al., 1998) and cannot be characterized uniquely. Therefore a range for interfacial toughness is assumed in this paper, based on two estimates of the interface fracture energy reported by He et al. (1998). The range of room temperature fracture energy varies from 10 $J m^{-2}$ for a diffusion interface to 1 $J m^{-2}$ for a degraded interface.

3.2. Geometric model and FEM mesh

A schematic diagram of the finite element model of the TBC system is shown in Fig. 3. Only straight sided and penny-shaped configurations are considered in this work and hence 2D plane strain and axi-symmetric representations of the TBC system are deemed sufficient. The TBC morphology and delamination are assumed to be symmetric about the vertical plane and only the half geometry is modeled. As shown in Fig. 3a, the delamination is characterized by a length parameter, which corresponds to a radius in the

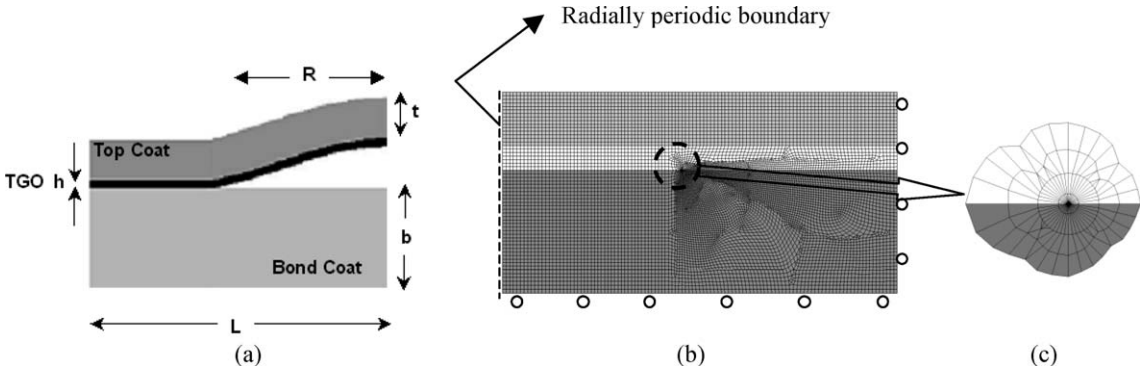

Fig. 3. Schematic diagrams showing (a) geometric and dimensional parameters, (b) finite element model of the TBC system with bond coat lower interface rigid, symmetry at vertical edge of delamination (right) and radial periodicity at the vertical edge of the bonded part (left), (c) close-up of the mesh at the crack tip.

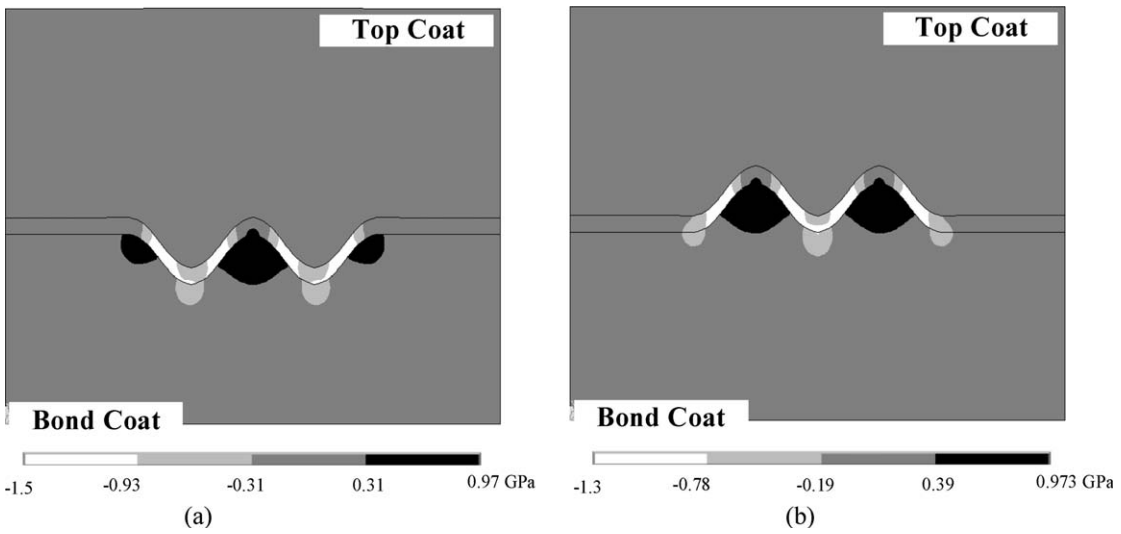

Fig. 4. Contour plots showing transverse stress (GPa) at fully bonded wavy interfaces for (a) Type I undulation penetrating completely into the bond coat, (b) Type II undulation protruding completely into the top coat.

axi-symmetric case or a width in plane strain. The bond coat-substrate interface is assumed to be relatively stress free, hence the substrate is not explicitly considered in this model. From Fig. 1 it can be observed that undulations in the vicinity of planar interfaces between the TGO and bond coat are commonly observed due to the surface roughness of the deposited bond coat. As demonstrated in Fig. 4, these undulations may penetrate into the bond coat (type I) or protrude completely into the top coat (type II). Other intermediate scenarios with undulations protruding into adjoining layers in various proportions are also possible. In this study, only sinusoidal undulations that correspond to the limiting configurations of Fig. 4 are considered.

The finite element model of a 100×80 μm TBC system consist of a mesh of four-noded (QUAD4) elements, identified as PLANE182 in the ANSYS element library (Ansys 7.0, 2003). These elements are capable of representing both plane strain and axi-symmetric behavior. The resulting model consist of more than 115,000 elements and 110,000 nodes, and exhibits less than 0.5% error in the strain energy when compared to a more refined mesh. As shown in Fig. 3c, a highly refined mesh is used in the vicinity of the crack-tip.

3.3. Boundary conditions

The TBC system model is subjected to a uniform thermal load through a drop in the temperature from 1000 °C to room temperature of 30 °C. The thermal loads caused by this cooling cycle generate compressive stresses in the TGO and top coat on account of CTE mismatch. For all buckling analyses a uniform thermal load creates the perturbation load in the system. Although temperature gradients are expected along the TBC thickness during service, the uniform thermal load assumption is considered adequate, since the critical buckling load is relatively insensitive to the perturbation load. For buckling analysis with planar or wavy interfaces, symmetry boundary conditions are applied at the left edge, roller supports are applied at the lower horizontal boundary to simulate a rigid substrate, and radial periodic boundary conditions are applied at the right edge of the models. The top surface of the TBC is exposed to the hot gases and is considered to be free of any mechanical constraints. The delaminated region is treated as a contact surface for the wavy interfaces only, and 2D surface contact elements are used in this region.

In the analysis of delamination growth by crack propagation at the wavy interface, symmetry boundary conditions are applied at the left edge, roller supports are applied at the lower horizontal boundary, and radial periodic boundary conditions are applied at the right edge of the models. The delaminated wavy interfaces have contact surfaces and surface contact elements are used in the calculation of energy release rate. Once again, temperature gradients are not considered in these simulations. The growth of delamination occurs primarily during the cooling cycle when the stresses due to CTE mismatch are the highest. The FEM simulations for the energy release rate are performed at room temperature.

4. Parametric modeling of buckling instability and interfacial crack extension

Simulations conducted with the computational models discussed in Section 2 are used to derive functional forms of the critical drivers of instability and crack extension induced damage in terms of important geometrical and material parameters in the TBC model. Sensitivity analyses of these drivers are conducted with respect to the parameters and the results are utilized in the determination of the functional dependence. Prior to the sensitivity analyses, model validation is conducted by comparing results of the simulations with analytical results in the literature.

4.1. Validation study of the computational model

The analytical solution of buckling instability in a two layer TBCs (bond coat and TGO) is provided by Hutchinson and Suo (1992). This work uses classical plate theory (CPT) with clamped edge constraints to obtain an analytical solution for the critical buckling stress:

$$\sigma_{\mathrm{b}} = \left[\frac{\pi^2 E}{12(1-\nu^2)}\right]\left(\frac{h}{R}\right)^2 \tag{5}$$

where σ_b is the critical buckling stress, E and ν are the elastic modulus and Poisson's ratio of the TGO, h is the TGO thickness, and R is the dimension of the existing delamination. Solutions of the finite element model are compared with those from Eq. (5). Although there is excellent agreement for $\frac{h}{R} \leqslant 0.06$, the results show divergence beyond this limit as shown in Fig. 5a. The discrepancy arises mainly from the limitations of the classical linear thin plate theory, implemented in the analytical solution. First, the assumption of a thin TGO in the delaminated region for smaller values of R may not be appropriate for higher (h/R) ratios. Higher order plate theories for thick plates, such as the one proposed by Reddy (1999), are deemed more appropriate for improved solutions. Secondly, the clamped plate theory with rigid rotational constraints at the edges is not a good approximation at higher values of (h/R). Since the TGO ligaments remain attached to the bond coat and have a finite stiffness in rotation, the debonded region does not behave as a clamped plate. The contribution and detachment of such ligaments under transverse loading have been discussed by Evans et al. (1999). On the other hand, the computational model captures the physics of the real problem, including the attached ligaments and rotational stiffness of the edges.

A special procedure is invoked to implement a higher order theory with elastically restrained edges in a more accurate representation of the analytical solution. It is observed that the computationally predicted buckling loads are within the extreme bounds of the Reddy plate theory calculations by Wang and Lee (1998) with zero and infinite rotational stiffness as summarized in Table 2. The rotational stiffness for the TBC system is calibrated through a comparison of the results of FEM simulations with the available analytical solutions by Wang and Lee (1998). The relation between Kirchhoff load and Reddy buckling load is given by Wang and Lee (1998) as:

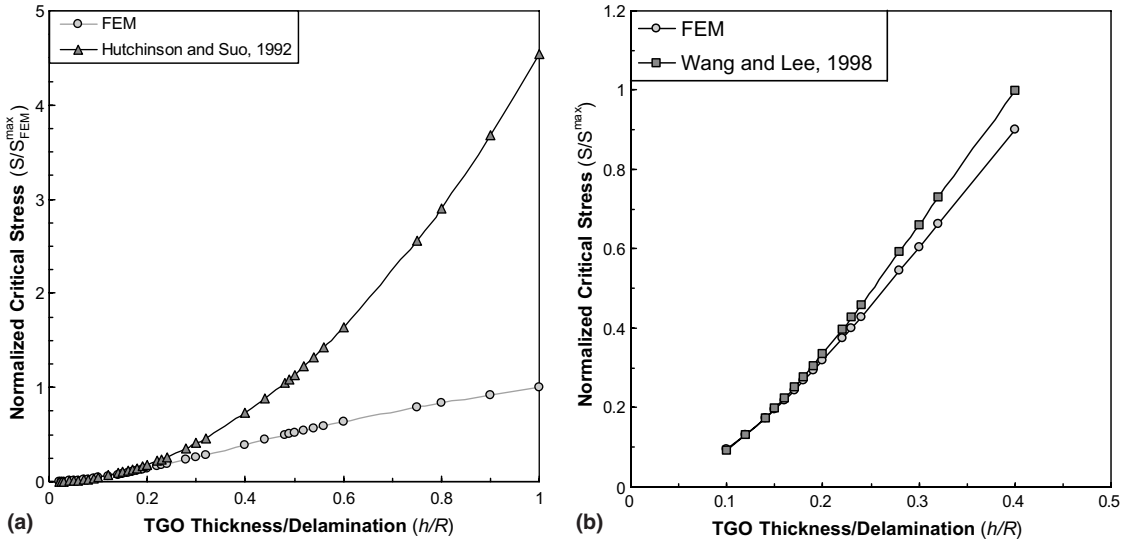

Fig. 5. Plots showing (a) the comparison between the finite element results and a low order analytical solution where normalizing stress $S^{\max}_{\mathrm{FEM}} = 110$ GPa, (b) comparison of finite element results and a higher order analytical solution where normalizing stress $S^{\max} = 46$ GPa.

Table 2
Critical buckling load comparison with results by Wang and Lee (1998)

h/R	FEM	Free edges (Wang and Lee, 1998)	Clamped edges (Wang and Lee, 1998)
0.2	10.16	5.64	17.7

$$N^{\mathrm{R}} = \frac{N^{\mathrm{K}}\left(1+\dfrac{N^{\mathrm{K}}}{70Gh}\right)}{\left(1+\dfrac{N^{\mathrm{K}}}{(14/17)Gh}\right)} \tag{6}$$

where G is the shear modulus and N^{R} and N^{K} represent the Reddy and Kirchoff buckling loads, respectively. Assuming the load N^{R} to be equal to the buckling load predicted by FEM solutions, N^{K} is solved from Eq. (6). The rotational stiffness parameter $\frac{K_r R}{D}$ is then evaluated from the unified Kirchoff equation (Wang and Lee, 1998)

$$\sqrt{\frac{N^{\mathrm{K}}R^2}{D}}J_0\left(\sqrt{\frac{N^{\mathrm{K}}R^2}{D}}\right)+\left(\frac{K_r R}{D}-(1-\nu)\right)J_1\left(\sqrt{\frac{N^{\mathrm{K}}R^2}{D}}\right)=0 \tag{7}$$

where, $D=\frac{Eh^3}{12(1-\nu^2)}$ is the flexural rigidity, R is the radius of the plate, and J_0 and J_1 are the Bessel functions of first kind of order zero and one, respectively. The value of rotational stiffness parameter is then used in Eq. (7) to obtain N^{K} for different values of R. Subsequently, the value of the buckling load may be evaluated from Eq. (6) for different values of (h/R) in the range $(0 \leqslant \frac{h}{R} \leqslant 1)$. Fig. 5b shows that the results obtained by this analytical model with higher order theory and finite rotational stiffness are in close agreement with the numerical results for values of $\frac{h}{R} \leqslant 0.2$. However, significant errors are still incurred at higher values of (h/R). This may be attributed to the use of a single data point used in the calibration of the

rotational stiffness parameter and the assumption that it remains constant throughout the entire range of (h/R). While limited studies have investigated plate buckling with different rotational stiffness (Lundquist and Stowell, 1942; Reismann, 1952; Wang and Lee, 1998), an established relationship between the rotational stiffness and the thickness, size, and modulus is lacking in the literature. Hence, the development of functional relations for buckling load for a larger range of (h/R) is pursued in this study. Such a functional form is needed, as large ratios are expected at the incipient stages of delamination formation and it is not known *a priori* whether the buckling instability initiates at such small delamination lengths.

4.2. Critical stress analysis for buckling instability in the TBC

The critical buckling load or stress is dependent on a number of geometric and material parameters of the TBC system, as well as on the applied loads. Deriving functional forms of the critical buckling loads in terms of the critical parameters is a desirable, yet non-trivial exercise. Simplified forms of such relations have been provided by Evans et al. (1997), He et al. (1998) and Hutchinson and Suo (1992). In this study, these relations are extended for more comprehensive accounting of the range of critical parameters. The relations are first developed for the two layered TBCs (bond coat and TGO) and subsequently extended to three-layered TBCs (bond coat, TGO, and ceramic top coat).

4.2.1. Two layer TBC system model

The first analysis is for a two-layered TBC with a planar interface. In order to identify the critical parameters entering the function, a sensitivity study of buckling load with respect to geometric and material parameters of the two layers is conducted for both plane strain and axi-symmetric conditions. Candidate parameters for this study are selected based on buckling characterization studies in the literature (e.g., Wright and Evans, 1999; Evans et al., 2001b; He et al., 1998; Hutchinson et al., 2000). The parameters considered in the sensitivity analysis are (i) L, length of the TBC model length, (ii) h, thickness of the TGO, (iii) b, thickness of the bond coat, (iv) E_{TGO}, stiffness of the TGO, (v) E_{BC}, stiffness of the bond coat, and (vi) R, length of the pre-existing delamination. Definitions of the geometric parameters are pictorially given in Fig. 3a.

In the FEM simulations of the TBC system for sensitivity analyses, a single parameter is varied at a time while keeping all others fixed. The results of the sensitivity analyses are summarized in Figs. 6a and b, where the normalized critical buckling stress is plotted as a function of the normalized geometric and material parameters, respectively. The critical buckling stressed for each case are normalized with respect to the corresponding maximum critical buckling stresses, i.e., $S^{\max} = 30.24$ GPa for the geometric parameters study and $S^{\max} = 0.52$ GPa for the material parameters study, respectively. Each parameter is normalized with its maximum value considered in this work, i.e., $L^{\max} = 1000$ μm, $b^{\max} = 100$ μm, $h^{\max} = 50$ μm, and $R^{\max} = 1000$ μm for geometric parameters and $E^{\max}_{\mathrm{TGO}} = 600$ GPa and $E^{\max}_{\mathrm{TC}} = 300$ GPa for material parameters. Fig. 6a shows very little influence of the overall model length L or the bond coat thickness b on the critical stress. The critical buckling stress decreases rapidly with increasing delamination length R before stabilizing at near zero critical buckling stress values. The critical stress variation is found to fit an inverse quadratic relation with the delamination length. When the two layers are completely delaminated ($R = L = 1000$ μm), the critical stress is equal to the buckling stress in a single layer. Finally, the critical stress increases nonlinearly with the TGO thickness h. The dependence is quadratic for lower TGO thicknesses, but for thicker TGOs the relation is more complex.

Fig. 6b summarizes the results of the sensitivity analyses with respect to the elastic moduli of the constituent materials of the TBC system. While the buckling stress is generally insensitive to the bond coat modulus, it reduces slightly (~8%) for a very compliant bond coat of approximately 1/20 of TGO modulus. For a compliant bond coat it is easier for the TGO to buckle at lower loads. This effect becomes significant when the modulus of bond coat is appreciably less than that of the TGO, as discussed by Cotterell and

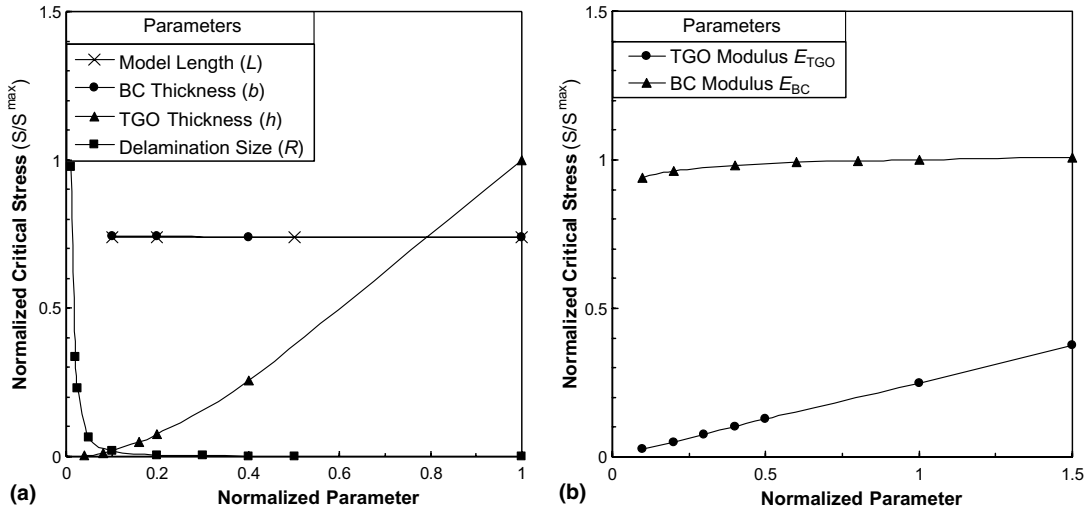

Fig. 6. Plots for the two layer TBC, showing critical buckling load sensitivity to (a) geometric parameters (normalizing values of $L^{\max} = 1000$ μm, $b^{\max} = 100$ μm, $h^{\max} = 50$ μm, $R^{\max} = 1000$ μm, and $S^{\max} = 30.2$ GPa), and (b) material parameters (normalizing values of $E_{\mathrm{TGO}}^{\max} = 600$ GPa, $E_{\mathrm{BC}}^{\max} = 600$ GPa, and $S^{\max} = 0.52$ GPa).

Chen (2000). For a compliant bond coat, the energy released from the bond coat has also been shown by Yu and Hutchinson (2002) to be much more than the energy stored in the TGO. The numerical model captures the reduction in critical stress for very compliant bond coat as predicted by analytical models (Cotterell and Chen, 2000; Yu and Hutchinson, 2002). The buckling stress is linearly dependent on the TGO modulus. When compared to plane strain delamination analyses, the sensitivity analyses for axi-symmetric delamination yields a self-similar functional dependence with a higher value for the critical stress.

4.2.2. Parametric representation of the critical stress for buckling instability

The sensitivity analysis forms a basis for the development of a parametric representation of the critical buckling stress $\sigma_{\mathrm{TGO}}^{b2}$ in terms of the important parameters for the two-layer TBC system. From the summary of results in Fig. 6, the critical parameters identified are the TGO thickness h, TGO modulus E_{TGO} and the interfacial delamination size R. Furthermore, it is also observed that a dependence of $\sigma_{\mathrm{TGO}}^{b2}$ on the (h/R) ratio best represents the influence of individual parameters h and R. This observation is also consistent with dimensional analysis. These analyses point to a functional form for the buckling stress as $\sigma_{\mathrm{TGO}}^{b2} \propto E_{\mathrm{TGO}} f((\frac{h}{R})^n)$ where n is a constant to be determined. A similar parametric dependence has been discussed by Evans et al. (1997) and He et al. (1998) as

$$\sigma_{\mathrm{TGO}}^{b2} = \begin{cases} 0.81 E_{\mathrm{TGO}} \left(\dfrac{h}{R}\right)^2 & \text{Plane strain} \\ 1.21 E_{\mathrm{TGO}} \left(\dfrac{h}{R}\right)^2 & \text{Axisymmetric} \end{cases} \tag{8}$$

These relations are based on the thin plate theory and consequently they have limited range of validity. It has been pointed out by Reddy (1999) that classical plate theory is valid for $0.0 < \left(\frac{h}{R}\right) \leqslant 0.05$, and the range of applicability is confirmed in the current FEM simulations as well. As shown in Fig. 5a, the analytical predictions are within 3% of the FEM results at $\left(\frac{h}{R}\right) = 0.06$. However, at higher (h/R) values, the two predictions diverge rapidly. For plane strain, the differences are 13%, 81% and 320% at (h/R) ratios of 0.2, 0.5

and 1.0, respectively. For the axi-symmetric case, the differences are 30%, 120% and 350%, respectively. From the present study, it is clear that $\sigma^{b2}_{\mathrm{TGO}}$ representation using a single continuous function of the parameters is very difficult.

Consequently, in the development of parametric relations for an extended range of validity, the range $0.0 < \left(\frac{h}{R}\right) \leqslant 1.0$ is divided into four segments. Each segment is determined from the nature of $\sigma^{b2}_{\mathrm{TGO}}$ dependence on the (h/R) ratio. Exclusive validity ranges are associated with each functional form to avoid non-unique solutions for any geometric configuration. For both the plane strain and axisymmetric cases, the first sub-domain corresponds to the range of validity of Eq. (8) derived by Evans et al. (1997) and He et al. (1998). The functional relations for the subsequent regions are obtained by a least squares based "best fit" analysis of the FEM solutions with an error tolerance of 3.5%. The parametric relations are summarized in Eqs. (9) and (10). Excellent agreement of these relations with the finite element results for the axisymmetric case is demonstrated in Fig. 7

$$\sigma^{b2}_{\mathrm{TGO}} = \begin{cases} 0.8100 E_{\mathrm{TGO}} \left(\dfrac{h}{R}\right)^{2} & \forall\ 0.00 < \left(\dfrac{h}{R}\right) \leqslant 0.06 \\ 0.4655 E_{\mathrm{TGO}} \left(\dfrac{h}{R}\right)^{1.8} & \forall\ 0.06 < \left(\dfrac{h}{R}\right) \leqslant 0.21 \\ 0.2765 E_{\mathrm{TGO}} \left(\dfrac{h}{R}\right)^{1.45} & \forall\ 0.21 < \left(\dfrac{h}{R}\right) \leqslant 0.50 \\ 0.2050 E_{\mathrm{TGO}} \left(\dfrac{h}{R}\right) & \forall\ 0.50 < \left(\dfrac{h}{R}\right) \leqslant 1.0 \end{cases} \quad \text{(for plane strain case)} \tag{9}$$

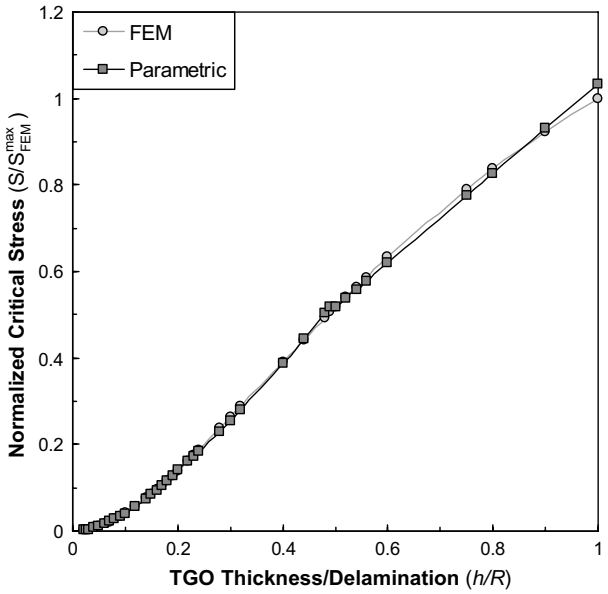

Fig. 7. Plots of the critical buckling stress as a function of h/R ratio for the two layer TBC, obtained with the parametric relations and finite element solution for the axisymmetric case (normalizing stress $S^{\max}_{\mathrm{FEM}} = 110$ GPa).

$$\sigma_{\mathrm{TGO}}^{b2} = \begin{cases} 1.2100 E_{\mathrm{TGO}} \left(\frac{h}{R}\right)^{2} & \forall\ 0.00 < \left(\frac{h}{R}\right) \leqslant 0.06 \\ 0.6800 E_{\mathrm{TGO}} \left(\frac{h}{R}\right)^{1.8} & \forall\ 0.06 < \left(\frac{h}{R}\right) \leqslant 0.21 \\ 0.3887 E_{\mathrm{TGO}} \left(\frac{h}{R}\right)^{1.45} & \forall\ 0.21 < \left(\frac{h}{R}\right) \leqslant 0.50 \\ 0.2753 E_{\mathrm{TGO}} \left(\frac{h}{R}\right) & \forall\ 0.50 < \left(\frac{h}{R}\right) \leqslant 1.0 \end{cases} \quad \text{(for axisymmetric case)} \tag{10}$$

These parametric equations do not suffer from the restrictive assumptions of the analytical solutions given by Hutchinson and Suo (1992), Evans et al. (1997) and He et al. (1998) and represent a wide range in the context of linear elasticity. It should be noted that the ranges of the (h/R) ratio are kept the same for both the plane strain and axisymmetric cases. Also, the exponents and the functional forms are kept the same with only differences in the coefficients. The distinct forms in different ranges result in discontinuities at the edges of the (h/R) ranges. The discontinuity errors are tabulated in Table 3 and are found to be within established limits. The slightly higher errors for the axisymmetric case are due to the fact that the range and exponents are kept the same as for the plane strain case.

4.2.3. Three layer TBC system model

The parametric form is subsequently extended for a three-layered TBC system consisting of the bond coat, TGO, and ceramic top coat with planar interfaces. A sensitivity analysis of the critical buckling load for this model is performed under plane strain assumptions only. In addition to h and R, the parameters include the top coat thickness (t) as shown in Fig. 3a, and the modulus (E_{TC}). Experimental observations by Wright and Evans (1999), Evans et al. (2001b) and Johnson et al. (1998) have motivated the consideration of the range of variation of t to be ~1–50 μm and of E_{TC} to be ~1–200 GPa. Fig. 8a summarizes the results of the sensitivity analysis with respect to t, h and R. In this analysis, $E_{\mathrm{TC}} = 100$ GPa, the normalizing top coat thickness $t^{\max} = 50$ μm and the normalizing stress $S^{\max} = 137$ GPa. The critical buckling stress increases sharply at lower values of the top coat thickness before stabilizing at a value that is significantly higher than the corresponding two-layer critical stress. This result concurs with the multi-layer analytical model predicting similar characteristics developed by Choi et al. (1999). Two important observations can be made from the plots in Fig. 8a. The stabilized critical stress depends on the TGO thickness h and is insensitive to the delamination size R. On the other hand, the rate of increase of the critical stress at lower values of t is inversely dependent on R and is insensitive to h. The magnification in $S/S^{\max}$ due to the addition of the top coat reduces with increasing (h/R) ratios (~4 for $h/R = 0.4$ and ~2 for $h/R = 0.8$). Furthermore, Fig. 8b shows a quadratic dependence of $S/S^{\max}$ on the elastic modulus E_{TC} for a fixed $(h/R) = 0.4$.

A process similar to that discussed for the two-layer TBC is followed to obtain a functional relation for critical buckling stress in the three-layer TBC. This functional relation reduces that in Eq. (9) in the limit that t is equal to zero. Using a least squares based "best fit" analysis of the FEM solutions with an error tolerance of 4%, this relation may be expressed as

Table 3
Discontinuities in the values of σ_b at the edges of each h/R ratio range in the parametric equations (9) and (10)

h/R ratio	Discontinuity error (%)	
	Plane strain	Axisymmetric
0.06	0.87	1.35
0.22	0.90	2.9
0.50	1.25	3.25

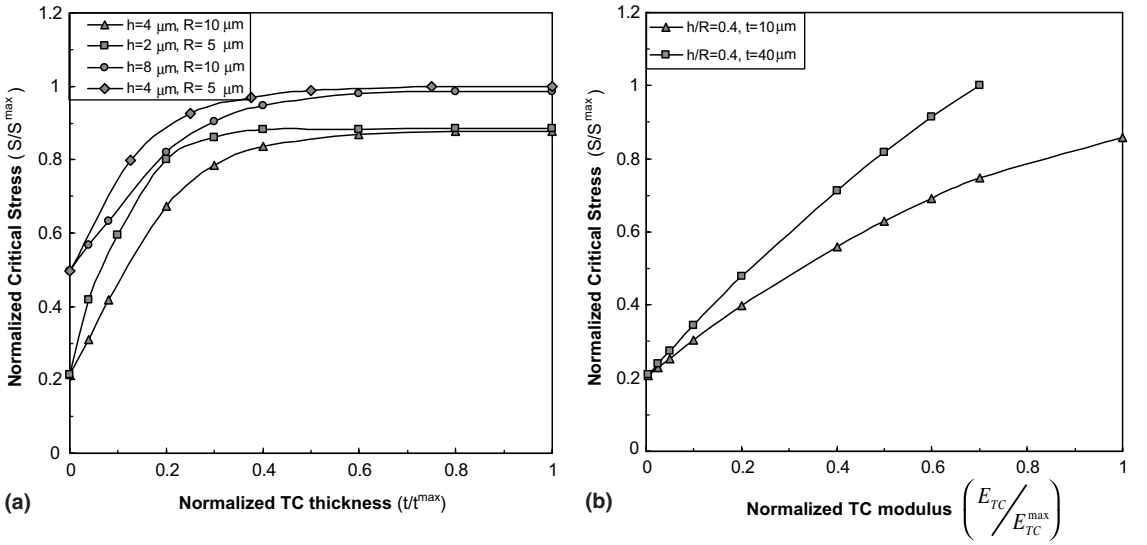

Fig. 8. Plots for the three layer TBC, showing the variation of normalized critical buckling stress with (a) top coat thickness (t) (normalizing values: $S^{\max} = 137$ GPa and $t^{\max} = 50$ μm) and (b) top coat modulus (E_{TC}) (normalizing values: $S^{\max} = 147$ GPa and $E_{\mathrm{TC}}^{\max} = 200$ GPa).

$$\sigma_{\mathrm{TGO}}^{b3} = \sigma_{\mathrm{TGO}}^{b2} + \left(\frac{h}{R}\right)^{-0.45}\left(1 - \mathrm{e}^{\left(C_1\frac{t}{R}\right)}\right)\left(C_2\frac{E_{\mathrm{TC}}^2}{E^*} + C_3 E_{\mathrm{TC}}\right) \quad \forall\ 0.25 \leqslant \left(\frac{h}{R}\right) \leqslant 1.0 \tag{11}$$

where $\sigma_{\mathrm{TGO}}^{b3}$ and $\sigma_{\mathrm{TGO}}^{b2}$ are the critical TGO stress for three and two layer TBCs respectively, $E^* = 1$ GPa (necessary for dimensional consistency) and C_1, C_2 and C_3 are constants. The constants are determined using the best fit analysis as: $C_1 = 1.115$, $C_2 = -1.33\mathrm{E}{-3}$ and $C_3 = 0.746$. Eq. (11) predicts the critical stress to within 4% of the FEM results for most parametric variations. However larger differences are found for $\left(\frac{h}{R}\right) < 0.25$ with maximum error 7.3% for $(h/R) = 0.2$ and hence, this formula is not recommended for such geometric configurations. Also top coats that are thinner than the TGO, i.e. $t < h$, are physically unlikely and are not considered in Eq. (11). This parametric form significantly improves the understanding of buckling instability in linearly elastic multi-layered TBCs and maybe used as a fail-safe design tool.

4.3. Estimating energy release rate for interfacial crack extension

It has been discussed in Section 2.2, that the presence of a wavy TGO-BC interface induces high transverse stresses perpendicular to the interface. Stress concentrations near the edge of a delamination may cause the delamination to extend, a phenomenon that is governed by the strain energy release rate. As shown by Hutchinson et al. (2000), this energy release rate in turn is influenced by various geometric and material parameters. Hence, it is desirable to develop comprehensive functional forms depicting the relation between the energy release rate and the critical parameters in TBC systems. Simplified parametric relations for two-layer TBCs have been provided by Evans et al. (1997) and He et al. (1998), among others, and for three-layer TBCs by Choi et al. (1999). However, these relations mainly address cracks propagating from undulations and exclude scenarios where the cracks propagate towards an interfacial undulation from a planar delaminated interface. The latter situation is considered in this paper with a realistic range of critical parameters.

The configurations in Fig. 4 describe the two limiting cases of wavy interfaces with undulations, protruding into alternate constituent layers. The type I undulation configuration penetrates the bond coat while the type II undulation configuration protrudes into the top coat. Finite element models of the two configurations with sinusoidal undulations are used for stress analysis in the 3-layer TBC system without any pre-existing delamination. The analyses conclude that the type I undulations induce tensile transverse stresses at the junction of planar and wavy interfaces, whereas the type II undulations induce compressive transverse stress at the same location as shown in the contour plots of Fig. 4. Consequently, the type I undulation configuration is chosen for developing parametric forms of the energy release rate. Only the plane strain case is considered in this study.

The first case considered in the development of the functional dependence is where the delamination is on the verge of extending into the wavy portion of the interface. Subsequently, the delamination is incrementally extended into the undulation and the variation of energy release rate is studied. A sensitivity analysis is done for the three-layer TBC system to assess the influence of critical parameters on the energy release rate G. Candidate parameters for this analysis are selected from results of characterization studies reported by Hutchinson et al. (2000), Choi et al. (1999) and Evans et al. (2001a,b). They are (i) TGO thickness (h), (ii) top coat thickness (t), (iii) length of the pre-existing delamination (R), (iv) amplitude of the sinusoidal undulation (A), (v) undulation wavelength (W), (vi) TGO stiffness (E_{TGO}), (vii) bond coat stiffness (E_{BC}), (viii) top coat stiffness (E_{TC}), and (ix) far-field thermal mismatch stresses σ_{TGO} and σ_{TC} in the TGO and the top coat, respectively. The ranges of each parameter are selected based on experimental observations by Tolpygo et al. (2001), Choi et al. (1999), Mumm et al. (2001), Tolpygo and Clarke (2000), Tolpygo and Clarke (2003) and Yanar et al. (2003) and are listed in Table 4. The far-field stress in a layer is evaluated as $(\alpha_{\mathrm{layer}} - \alpha_{\mathrm{substrate}})\Delta T$, where α is the coefficient of thermal expansion and ΔT is the temperature change from the stress free state. Since the far field stress is a linear function of ΔT, its variation is achieved by simply reducing the applied uniform temperature in a range from 900 °C to 30 °C, assuming that 1000 °C is the stress free temperature.

The sensitivity analysis is carried out by varying a single parameter at a time. The analysis shows highly nonlinear dependence of the energy release rate G on some parameters like h, A, and W. More variations of these nonlinear parameters are considered in the sensitivity simulations. The energy release rate G is calculated by the virtual crack extension method discussed in Section 2.2. Results of the sensitivity analysis are summarized through plots of the variation of the normalized energy release rate $G/G^{\max}$ with normalized geometric and material parameters in Figs. 9 and 10. For each plot, $G^{\max}$ is calculated from the FEM analyses and the normalizing parameters are $h^{\max} = 6\ \mu\mathrm{m}$, $t^{\max} = 15\ \mu\mathrm{m}$, $E^{\max}_{\mathrm{TGO}} = 480$ GPa, $E^{\max}_{\mathrm{TC}} = 80$ GPa, $E^{\max}_{\mathrm{BC}} = 280$ GPa, $A^{\max} = 10\ \mu\mathrm{m}$, $W^{\max} = 30\ \mu\mathrm{m}$, and $R^{\max} = 35\ \mu\mathrm{m}$. Fig. 9a shows that $G/G^{\max}$ varies inversely with t, prior to stabilizing at a constant value. It also shows a non-linear dependence for lower values of h. Fig. 9b shows that $G/G^{\max}$ has a strong dependence on E_{TC} and E_{TGO}; increasing linearly with E_{TGO} and

Table 4
Range of variation of parameters from experimental observations by Tolpygo et al. (2001), Choi et al. (1999), Mumm et al. (2001), Tolpygo and Clarke (2000), Tolpygo and Clarke (2003) and Yanar et al. (2003) for energy release rate study

Parameter	Range of variation
TGO thickness (h)	1–6 μm
Undulation amplitude (A)	5–10 μm
Undulation wavelength (W)	10–30 μm
Interfacial delamination (R)	5–70 μm
Top coat modulus (E_{TC})	10–100 GPa
TGO modulus (E_{TGO})	260–480 GPa
Bond coat modulus (E_{BC})	150–280 GPa

All combinations of A and W, outside of the range $0.3 < \frac{A}{W} < 0.5$ are excluded.

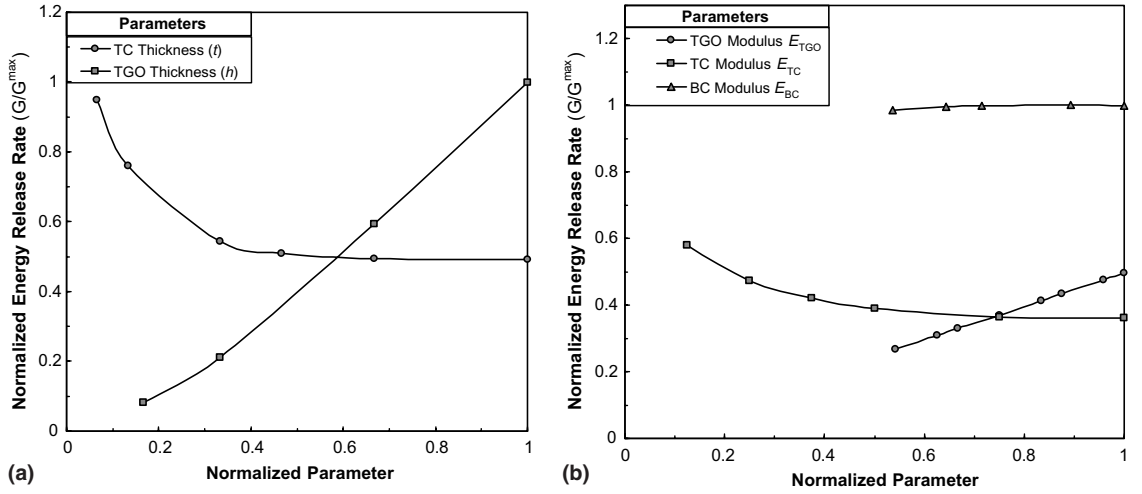

Fig. 9. Plot showing the sensitivity of the energy release rate with respect to (a) geometric parameters (normalizing measures are $h^{\max} = 6\ \mu\text{m}$, $t^{\max} = 15\ \mu\text{m}$, and $G^{\max} = 22\ \text{J/m}^2$), and (b) material parameters (normalizing measures are $E_{\text{TGO}}^{\max} = 480\ \text{GPa}$, $E_{\text{TC}}^{\max} = 80\ \text{GPa}$, $E_{\text{BC}}^{\max} = 280\ \text{GPa}$, and $G^{\max} = 12\ \text{J/m}^2$).

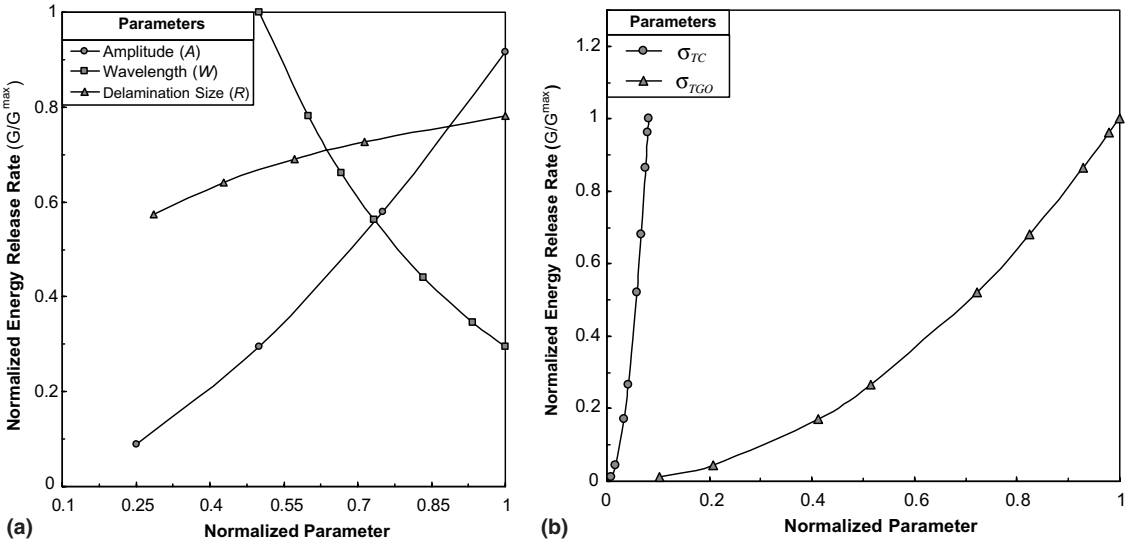

Fig. 10. Plot showing the sensitivity of the energy release rate with respect to (a) undulation parameters (normalizing factors are $A^{\max} = 6\ \mu\text{m}$, $W^{\max} = 30\ \mu\text{m}$, $R^{\max} = 35\ \mu\text{m}$, and $G^{\max} = 16\ \text{J/m}^2$), (b) expansion mismatch stress in the TGO and top coat (normalizing factors are $\sigma^{\max} = 2.2\ \text{GPa}$ and $G^{\max} = 4.6\ \text{J/m}^2$).

decreasing asymptotically with E_{TC}. However, it is relatively insensitive to E_{BC} and is only about 7% smaller than the maximum value for a very compliant bond coat ($E_{\text{BC}}^{\min} \sim 100\ \text{GPa}$). Hence E_{BC} is excluded from the expression of the parametric relation. Fig. 10 shows the sensitivity of $G/G^{\max}$ with respect to the geometric parameters of the undulation. It has an inverse non-linear dependence on the wavelength (W) and a non-linear dependence on the amplitude (A). The influence of the delamination size (R) is relatively weak.

Table 5
Functional relation between energy release rate and critical parameters, based on sensitivity analysis using FEM simulations

Function of (parameters)	Functional relation to G
$f_1(h, A, W)$	$\left(c_1\frac{h^2}{h_0}+c_2h+c_3\right)\left(\tan^{-1}\left(\frac{2\pi A+3h}{W}\right)\right)^{c_4}$
$f_2(t)$	$c_5te^{-c_6\frac{t}{t_0}}+c_7$
$f_3(R)$	$c_6\left(1-e^{c_7\frac{R}{R_0}}\right)$
$f_4(\sigma_{TC}, E_{TC}, \sigma_{TGO}, E_{TGO})$	$\left(c_8\frac{\sigma_{TGO}^2}{E_{TGO}}+c_9\frac{\sigma_{TC}^2}{E_{TC}}e^{c_{10}\frac{E_{TC}}{E^*}}\right)$

The values h_0, t_0, R_0, E^* and c_n ($n = 1$–10) are constants that are determined using the least square fit technique.

Also G/G^{max} is found to be very sensitive to the far field stresses σ_{TGO} and σ_{TC} with quadratic dependences as shown in Fig. 10(b).

4.3.1. Parametric representation of the energy release rate

Based on their influence on the energy release rate G, the critical parameters are re-classified into four basic groups and the sensitivity study results are used to establish their functional relations. The functional relation for each group is expressed in Table 5. The constant values h_0, t_0, R_0, E^* and c_n (for $n = 1$–10) in these relations are determined by using the least square fit with data generated by FEM simulations. These functions are subsequently combined to derive a functional dependence form of the energy release rate as

$$G \propto f_1(h, A, W) f_2(t) f_3(R) f_4(\sigma_{TGO}, E_{TGO}, \sigma_{TC}, E_{TC}) \tag{12}$$

This combined function is constrained to have a zero value, when: (i) the system is stress free, (ii) the TGO and the top coat thickness or their elastic moduli reduce to zero simultaneously (i.e., $h = t = 0$ or $E_{TGO} = E_{TC} = 0$), (iii) there is no delamination ($R = 0$) and (iv) there is no interfacial undulation in the vicinity of the delamination ($A = 0$ or $W = \infty$). The energy release rate should not become zero when only one of the TGO or top coat thicknesses or moduli reduces to zero (i.e., $h \neq t = 0$ or $E_{TGO} \neq E_{TC} = 0$). From these constraint considerations, the energy release rate functional form is derived to be

$$G = (\tan^{-1}\psi)^{C_1}\left(C_2te^{-C_3\frac{t}{t_0}} - C_4\frac{h^2}{h_0} + C_5h\right)\left(1-e^{-C_6\frac{R}{R_0}}\right)\xi\sigma_{TGO}^2 \tag{13}$$

where

$$\psi = \left(\frac{2\pi A + 3h}{W}\right), \quad \xi = \left(C_7\frac{1}{E_{TGO}} + C_8\frac{(\alpha_{TC}-\alpha_{BC})^2E_{TC}}{(\alpha_{TGO}-\alpha_{BC})^2E_{TGO}^2}e^{-C_9\frac{E_{TC}}{E^*}}\right)$$

$t_0 = 1$ μm, $h_0 = 1$ μm, $R_0 = 1$ μm, $E^* = 1$ GPa, ($\alpha_{layer}-\alpha_{BC}$) is the CTE mismatch of the layers and C_1–C_9 are constants. The constants in Eq. (13) are evaluated using a least squares based best fit analysis of the FEM results with a tolerance of 10%. For stresses and moduli expressed in GPa, lengths in μm, and the energy release rate in J/m^2, the constants are derived to be: $C_1 = 3.62$, $C_2 = 2.02\times10^3$, $C_3 = 0.92$, $C_4 = 17.83$, $C_5 = 427.97$, $C_6 = 0.14$, $C_7 = 1.10$, $C_8 = 111.25$ and $C_9 = 0.12$. This relation is found to predict energy release rate to within 6% of the all simulation results for a wide range of parametric variations. Only for TBC systems with a very thin top coat (i.e. $t < 10$ μm), the maximum error is relatively high and ~10%. Larger differences between FEM results and the predicted values are also found when the amplitude (A) is significantly less than the TGO thickness (h), which are taken to be out of the validity range for this relation.

An alternate mechanism of crack propagation has been suggested by Xu et al. (2004) for flat interfaces. This requires an interfacial delamination to originate from the root of a vertical cleavage crack penetrating through the top coat and the TGO. An analytical solution for steady state energy release rate at such an edge delamination has been derived by Xu et al. (2004) as

$$G_{ss} = \frac{\sigma_{TGO}^2 h_{TGO}(1-\nu^2)}{2E_{TGO}} + \frac{\sigma_{TC}^2 h_{TC}(1-\nu^2)}{2E_{TC}} - \sum_{i=TGO,TC} \frac{1}{E_i}\left[\frac{P^2}{h_i} + \frac{12M_i^2}{h_i^3}\right] \tag{14}$$

with

$$P = \frac{E_{TC}h_{TC}^2}{6}\kappa, \quad M_i = \frac{E_i \kappa h_i^3}{12} \quad \text{and} \quad \kappa = \frac{3(\varepsilon_{TGO} - \varepsilon_{TC})}{2h_{TC}\left[1 + \frac{E_{TC}h_{TC}}{4E_{TGO}h_{TGO}}\right]},$$

where σ_i and ε_i denote the expansion mismatch stress and strain, h_i denotes thickness, E_i is the elastic modulus of the respective layers and ν is the Poisson ratio of the TGO and the top coat. It is demonstrated by Xu et al. (2004) that G_{ss} for such a delamination can reach very high values and grow even for fairly tough interfaces. Fig. 11 shows a comparison of G from Eq. (13) with G_{ss} from Eq. (14) for a TBC with 10 μm thick top coat. In the vicinity of a significant undulation, G exceeds the value of G_{ss}. Despite predicting comparable energy release rates for specific configurations, there are several notable differences between the functional forms of Eqs. (13) and (14). These are as follows.

(i) The energy release rate at an edge delamination in Eq. (14) increases almost linearly with top coat thickness (t). However, for the case of a delamination in the vicinity of an interfacial undulation, G decreases exponentially before stabilizing at a constant value. This difference may be attributed

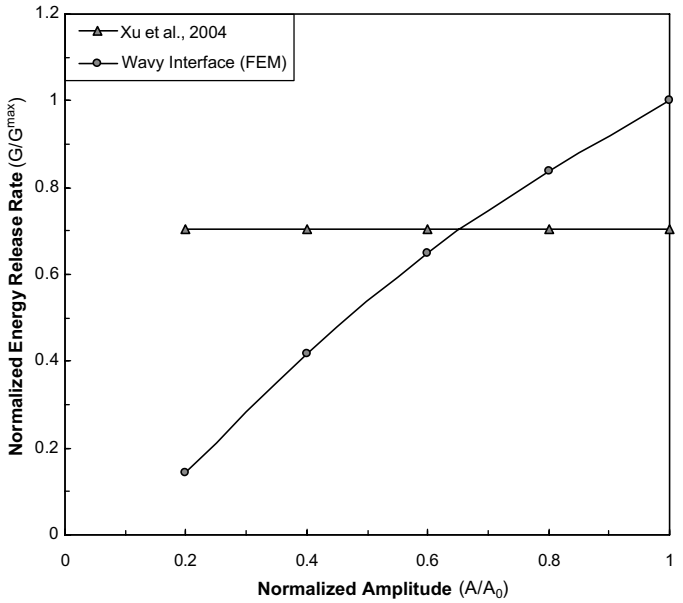

Fig. 11. Plot showing the comparison of energy release rate (G) near an interfacial undulation with the steady state energy release rate (G_{ss}) at an edge delamination (Xu et al., 2004) for $h/R = 0.2$, $t = 10$ μm, $W = 30$ μm and $\sigma_{TGO} = 2.17$ GPa (normalizing factors: $A_0 = 10$ μm, $G^{max} = 52$ J/m^2).

to the symmetry constraint imposed on the detached bi-layer that limits it from acquiring a curvature comparable to that of the edge delamination. The sensitivity analysis predicts that this constraint increases with increasing top coat thickness and elastic modulus, before stabilizing at a constant value. This characteristic difference reveals that for a thicker top coat, the prediction of higher G_{ss} by Eq. (14) is more appropriate than that by Eq. (13).

(ii) The Eq. (14) shows that at an edge delamination, both the detached layers have comparable contribution to the energy release rate, whereas Eq. (13) suggests that near an undulation the TGO layer contribution outweighs the exponentially decreasing contribution of the top coat. Hence, the stress state in the TGO layer is more critical for the G of delaminations near undulations.

For any given geometric configuration and materials properties, the energy release rate reaches a critical value G^c when the far field stress in the TGO reaches a critical value (σ^c_{TGO}). The corresponding parametric equation for the critical TGO stress is obtained from Eq. (13) as

$$\sigma^c_{TGO} = \left(\frac{G^c}{(\tan^{-1}\psi)^{C_1}\left(C_2 t e^{-C_3\frac{L}{t_0}} - C_4\frac{h^2}{h_0} + C_5 h\right)\left(1 - e^{-C_6\frac{R}{R_0}}\right)\xi} \right)^{0.5} \tag{15}$$

Eq. (15) reveals that for delamination growth, σ^c_{TGO} varies inversely with TGO thickness and with the delamination size. The critical stress σ^c_{TGO} also varies with the inverse of the CTE mismatch, and hence a larger mismatch will assist delamination. The CTE mismatch should therefore be minimized to extend TBC life.

As an extension to the present sensitivity analysis, the energy release rate is determined for an interfacial delamination extending into the undulation region. Fig. 12 shows that the energy release rate increases as the delamination extends over the first quarter of the undulation wave and then reduces to minimum (G^{min}) at the beginning of the last quarter. Comparing the values at the beginning and end of the entire undulation period, it is seen that G ends up higher after the delamination has extended over an undulation. This observation confirms its dependence on the delamination length as predicted by the sensitivity analysis. From

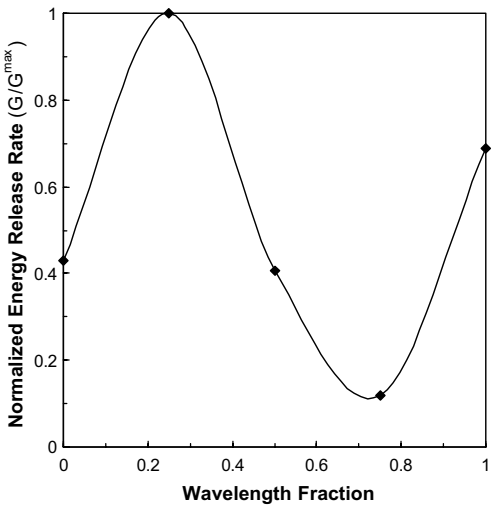

Fig. 12. Plot showing the variation of the normalized energy release rate as the interfacial crack propagates along an interfacial undulation for $W = 20$ μm, $A = 4$ μm and $G^{max} = 21$ J/m^2.

this study it is apparent that for any undulation, if $G^{\min}$ exceeds interface strength, delamination may extend completely over it.

5. Competition between buckling and crack extension modes

The parametric forms of Eqs. (11) and (15) predict the critical stresses $\sigma^{b3}_{\mathrm{TGO}}$ and $\sigma^{c}_{\mathrm{TGO}}$ for buckling instability and interface crack extension respectively, in a three-layer TBC. For any given configuration, material and load condition, the critical stress can therefore be determined for each mechanism. A comparative analysis using these equations can determine optimal configurations for the TBC system from a fail-safe point of view. Such a comparison is clearly limited to the delamination approaching an undulation from a flat interface.

To study the competition between these failure mechanisms as the delamination extends over an undulation, a FEM model of a representative TBC configuration is set up with the following parameters: $h = 1$ μm, $t = 5$ μm, $A = 4$ μm, $W = 20$ μm, $R = 30$ μm, $E_{\mathrm{TC}} = 40$ GPa and $E_{\mathrm{TGO}} = 400$ GPa. Since the delaminated wavy surfaces can come in contact and alter the buckling mode shape as well as G, these surfaces are modeled using contact elements in the FE model. The competition of the two modes is best understood from the results of the simulations in the form of the graphical representation in Fig. 13. The critical stress $\sigma^{\mathrm{cw}}_{\mathrm{TGO}}$ at which G exceeds the critical interface energy G^{c} in Eq. (15) is compared with the critical buckling stress $\sigma^{\mathrm{bw}}_{\mathrm{TGO}}$. The four plots represent the energy release rates G for a temperature drop from 1000 °C to room temperature (30 °C), for four different locations of the crack tip as shown in Fig. 13b. The vertical dotted lines represent the critical buckling stress $\sigma^{\mathrm{bw}}_{\mathrm{TGO}}$ corresponding to the four crack tip locations, while the dashed horizontal lines enclose the range of possible interfacial fracture energies for such configuration from the data given by He et al. (1998). For a weak interface with fracture energy 1 J/m^2, $\sigma^{\mathrm{cw}}_{\mathrm{TGO}}$ is lower than $\sigma^{\mathrm{bw}}_{\mathrm{TGO}}$ for all configurations and loading conditions, and hence delamination dominates. The competition is more pronounced for a strong interface (fracture energy = 10 J/m^2) and is investigated for crack tip locations **a**, **b, c** and **d** in Fig. 13b. The selection of these locations is based on the variation of G with crack advance shown in Fig. 12.

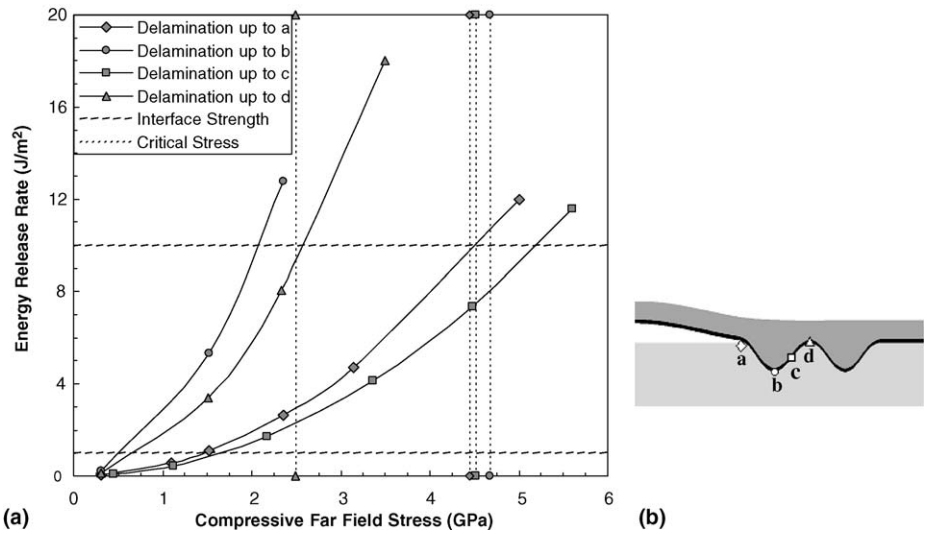

Fig. 13. Plot showing (a) the competition between buckle initiation and interface crack extension, (b) the corresponding locations for energy release rate curves and for study of the competition between buckling and delamination propagation.

As the delamination approaches the undulation wave at location **a**, σ_{TGO}^{cw} marginally exceeds buckling stress and the crack will extend to location **b** where the slope of the undulation reverses. At location **b**, σ_{TGO}^{cw} reduces considerably but σ_{TGO}^{bw} is slightly higher due to the thicker bending cross-section. Consequently, the crack extends to location **c** where σ_{TGO}^{cw} is expected to be maximum. The buckling instability dominates here since σ_{TGO}^{bw} is significantly lower than σ_{TGO}^{cw}. Beyond location **c**, σ_{TGO}^{cw} is expected to reduce but a comparison at location **d** shows σ_{TGO}^{bw} is slightly lower than σ_{TGO}^{cw} and hence buckling still dominates. From these numerical results, it is apparent that buckling instability is most likely to occur when the delamination is either at a planar interface or reaches the last quarter of an undulation. For other cases, interfacial crack extension mode dominates, especially when the undulation amplitude is significant.

6. Conclusions

In this paper, characteristics of failure modes e.g. buckling instability and strain energy driven interfacial crack propagation at interfacial delamination in linear elastic thermal barrier coatings (TBCs) are investigated using a finite element model. The solution of a linear elastic eigen-value problem determines the onset of the buckling instability with a pre-existing delamination between bond coat and the TGO. The virtual crack extension method is employed to study strain energy release rate driven interfacial delamination at wavy interfaces. The materials and geometries in the study are chosen to be representative of TBC materials in real applications. Extensive sensitivity analyses are conducted to identify the critical design parameters affecting the onset of buckling and extension of interfacial delamination, as well as to develop parametric relations that enhance the understanding of these mechanisms. These novel parametric relations, that extend the range of applications of the functional dependence found in literature, are validated with existing relations in the literature.

The paper concludes with a numerical exercise studying the competing mechanisms as the delamination extends over an undulation. It is demonstrated that the buckling instability is the leading failure mechanism at flat interfaces or near the locations of minimum cross-section in a wavy interface. However, in the vicinity of waviness, crack extension can become a dominant mode of failure. The probability of a particular mechanism taking precedence over the other depends on various geometric and material parameters and the nature of the loading. A comparative study of the predicted critical buckling stress with critical delamination stress can identify the dominant mechanism. The highlights of studies with these parametric relations are summarized below.

- The critical buckling stress relationships for two-layer TBCs has an extended range of validity and better accuracy for incipient stages of buckling instability as compared to the existing analytical solutions in the literature (Evans et al., 1997; He et al., 1998). The effect of the top coat is realized through its inclusion in the three-layer TBC model. The critical stress for this model is found to strongly dependent on the top coat geometry and material, in addition to the relevant two layer model parameters. The effect of the top coat thickness is found to stabilize with increasing thickness.
- The parametric form for the critical stress initiating interfacial crack extension at the delamination in a three-layer TBC is vital for understanding the effect of interface morphology on the failure mechanism. Furthermore, it is helpful in quantitatively establishing criteria for dominant failure mechanisms.
- The parametric relations can be used by designers as a helpful tool in the design of reliable TBCs in thermo-mechanical applications. The life of TBCs can be prolonged through an optimal combination of geometric and material parameters that suppresses the dominant mechanism.

Although the present study illustrates the competition between the failure mechanisms in detail, the validity is limited to the linear elastic TBCs. The failure modes will be further influenced by the material

non-linearity of the constituent layers, cyclic thermal loading and residual stresses, and this is the subject of a subsequent paper.

Acknowledgements

The authors are grateful for the support provided by the National Aeronautics and Space Administration (NASA) through a University Research Engineering Technology Institute (URETI) grant to the Ohio State University for Aeropropulsion and Power Technology (UAPT). Computer support by the Ohio Supercomputer Center through grant PAS813-2 is also gratefully acknowledged.

References

Ansys7.0, X., 2003. Structural Analysis Guide, Ansys Inc., USA.

Cheng, J., Jordan, E.H., Barber, B., Gell, M., 1998. Thermal/Residual stress in an electron beam physical vapor deposited thermal barrier coating system. Acta Materialia 46 (16), 5839–5850.

Choi, R.S., Hutchinson, J.W., Evans, A.G., 1999. Delamination of multilayer thermal barrier coatings. Mechanics of Materials 31, 431–447.

Cook, R.D., Malkus, D.S., Plesha, M.E., 1989. Concepts and Applications of FE Analysis. John Wiley & Sons, New York.

Cotterell, B., Chen, Z., 2000. Buckling and cracking of thin films on compliant substrates under compression. International Journal of Fracture 104, 169–179.

Evans, A.G., He, M.Y., Hutchinson, J.W., 1997. Effect of interface undulations on the thermal fatigue of thin films and scales on metal substrates. Acta Materialia 45 (9), 3543–3554.

Evans, A.G., Hutchinson, J.W., He, M.Y., 1999. Micromechanics model for the detachment of residually compressed brittle films and coatings. Acta Materialia 47 (5), 1513–1522.

Evans, A.G., He, M.Y., Hutchinson, J.W., 2001a. Mechanics-based scaling laws for the durability of thermal barrier coatings. Progress in Materials Science 46, 249–271.

Evans, A.G., Mumm, D.R., Hutchinson, J.W., Meier, G.H., Pettit, F.S., 2001b. Mechanisms controlling the durability of thermal barrier coatings. Progress in Materials Science 46, 505–553.

He, M.Y., Evans, A.G., Hutchinson, J.W., 1998. Effects of Morphology on the decohesion of compressed thin films. Physica Status Solidi A 166, 19–35.

Hutchinson, J.W., He, M.Y., Evans, A.G., 2000. The influence of imperfections on the nucleation and propagation of buckling driven delaminations. Journal of the Mechanics and Physics of Solids 48, 709–734.

Hutchinson, J.W., Suo, Z., 1992. Mixed mode cracking in layered materials. Advances in Applied Mechanics 29, 148–165.

Johnson, C.A., Ruud, J.A., Bruce, R., Wortman, D., 1998. Relationship between residual stress, microstructure and mechanical properties of electron beam-physical vapor deposition thermal barrier coatings. Surface and Coatings Technology 108-109, 80–85.

Lundquist, E.E., Stowell, E.Z., 1942. Critical compressive stress for flat rectangular plates supported along all edges and elastically restrained against rotation along the unloaded edges. In: National Advisory Committee for Aeronautics Report No. 733, pp. 99–109.

Mumm, D.R., Evans, A.G., Spitsberg, I.T., 2001. Characterization of a cyclic displacement instability for a thermally grown oxide in a thermal barrier system. Acta Materialia 49, 2329–2340.

Pan, D., Chen, M.W., Wright, P.K., Hemker, K.J., 2003. Evolution of a diffusion aluminide bond coat for thermal barrier coatings during thermal cycling. Acta Materialia 51, 2205–2217.

Parks, D.M., 1974. A stiffness derivative finite element technique for determination of crack tip stress intensity factors. International Journal of Fracture 10 (4), 487–502.

Reddy, J.N., 1999. Elastic Plates: Theory and Analysis. Taylor & Francis, Philadelphia, PA.

Reismann, H., 1952. Bending and buckling of an elastically restrained circular plate. Journal of Applied Mechanics, 167–171.

Tolpygo, V.K., Clarke, D.R., 2000. Surface rumpling of a (Ni,Pt)Al Bond coat induced by cyclic oxidation. Acta Materialia 48, 3283–3293.

Tolpygo, V.K., Clarke, D.R., 2003. Morphological evolution of thermal barrier coatings induced by cyclic oxidation. Surface and Coatings Technology 163–164, 81–86.

Tolpygo, V.K., Clarke, K.S., Murphy, K.S., 2001. Oxidation-induced failure of EB-PVD thermal barrier coatings. Surface and Coatings Technology 146–147, 124–131.

Wang, J.S., Evans, A.G., 1998. Measurement and analysis of buckling and buckle propagation in compressed oxide layers on superalloy substrates. Acta Materialia 46 (14), 4993–5005.

Wang, C.M., Lee, K.H., 1998. Buckling load relationship between Reddy and Kirchhoff Circular plates. Journal of the Franklin Institute 335 (6), 989–995.

Wright, P.K., Evans, A.G., 1999. Mechanisms governing the performance of thermal barrier coatings. Current Opinions in Solid State and Material Science 4, 255–265.

Xu, T., Faulhaber, S., Mercer, C., Maloney, M., Evans, A.G., 2004. Observations and analyses of failure mechanisms in thermal barrier systems with two phase bond coats on NiCoCrAlY. Acta Materialia 52, 1439–1450.

Yanar, N.M., Kim, G., Hamano, S., Pettit, F.S., Meier, G.H., 2003. Microstructural characterization of the failures of thermal barrier coatings on Ni-based supperalloys. Materials at High Temperatures 20 (4), 495–506.

Yu, H.H., Hutchinson, J.W., 2002. Influence of substrate compliance on buckling delamination of thin films. International Journal of Fracture 113, 39–55.